Superconducting flip-chip devices using indium microspheres on Au-passivated Nb or NbN as under-bump metallization layer

Achintya Paradkar, Paul Nicaise, Karim Dakroury, Fabian Resare, and Witlef Wieczorek, Department of Microtechnology and Nanoscience (MC2), Chalmers University of Technology, SE-412 96 Gothenburg, Sweden

Superconducting flip-chip interconnects are crucial for the three-dimensional integration of superconducting circuits in sensing and quantum technology applications. We demonstrate a simplified approach for a superconducting flip chip using commercially available indium microspheres and an in-house-built transfer stage for bonding two chips patterned with superconducting thin films. We use a gold-passivated niobium or niobium nitride layer as an under-bump metallization (UBM) layer between an aluminum-based superconducting layer and the indium interconnect. At millikelvin temperatures, our flip-chip assembly can transport a supercurrent with tens of milliamperes, limited by the smallest geometric feature size and critical current density of the UBM layer. We also show that the indium interconnect itself can carry a supercurrent exceeding 1 A. Our flip-chip assembly does not require patterning and electroplating of indium, nor does it need a flip-chip bonder. Thus, the presented flip-chip devices can be utilized in applications that require few superconducting interconnects carrying large currents at millikelvin temperatures.

I. INTRODUCTION

Superconducting flip-chip interconnects are pivotal in the integration of superconducting circuits for quantum computing [1-5] and sensing applications [6, 7]. A commonly used method employs indium (In) bump bonding as indium is superconducting below 3.4 K, ductile [8], and mechanically stable at cryogenic temperatures [1, 2, 7], resilient to thermal cycling [1], and reduces thermal stress between the top and bottom chips [8, 9]. However, indium as a bonding material may diffuse into certain superconducting thin films, potentially degrading their superconducting properties. This issue arises when indium is bonded to aluminum (Al), which results in an intermetallic compound that exhibits non-superconducting behavior [10]. Therefore, a commonly used method is to add an under-bump metallization (UBM) layer between the In and Al layers to prevent this diffusion. The UBM layer is usually made with superconductors such as niobium nitride [4, 11] or titanium nitride [1, 12]. The UBM layer forms a native oxide that must be removed before indium microbumps are deposited to make galvanic con-

Indium microbumps are typically grown via electroplating [9, 13] or evaporation [1, 4, 5, 13] and face-to-face compression bonded using a flip-chip bonder [1, 4, 5, 14, 15]. This technique is used in high-density three-dimensional packaging of integrated superconducting qubit processors, which require a small bump area to accommodate a large number of connections and a small (spacing $\leq 10\,\mu\text{m}$) and uniform (tilt $\leq 100\,\mu\text{rad}$) chip separation for scalability [4, 5]. However, this approach requires an elaborate fabrication process and a high-precision flip-chip bonder. Alternative flip-chip bonding techniques have been developed to mitigate this problem

[3, 16], but they do not provide galvanic contact.

In our work, we present a simplified fabrication and assembly process for making a superconducting flip-chip connection between a superconducting Al layer, which is a commonly used material for superconducting quantum circuits [1, 2, 4, 5], and a superconducting niobium nitride (NbN) or niobium (Nb) layer as the UBM layer. Our flip-chip assembly can carry a supercurrent of tens of mA at temperatures in the range of a few tens of millikelyin to 1.2 K, i.e., the superconducting transition of Al. Our approach targets applications that require only a few superconducting connections, allowing for a larger indium bump size. We demonstrate that superconducting flip-chips can be assembled using commercially available 300 µm diameter indium microspheres [17] as the bond connection, which themselves can carry a supercurrent of more than 1 A. The microspheres are placed manually on a bottom chip immediately before pressing the bottom and a top chip together using a simple transfer stage [18].

Our flip-chip approach uses indium microspheres, eliminating the need for patterning and growing indium microbumps. To connect to a superconducting Al thin film, we demonstrate flip-chip assemblies with the commonly used NbN [4, 11]. Importantly, we also show that Nb can be used as a UBM layer, provided that it is capped with a thin Au layer to prevent oxidization. We choose Nb specifically because it exhibits a higher critical current density, which enables high current devices such as on-chip magnetic traps [19, 20] or on-chip solenoids [21], and its lower intrinsic microwave losses are promising for high-Q superconducting resonators [22, 23]. Au is chosen as the passivation layer because it mechanically strengthens the flip-chip bond [24], and if an Au-In intermetallic compound is formed, it would also be superconducting at millikelvin temperatures [25]. Our flip-chip assembly can find applications, among others, as an on-chip flux transformer for remote sensing of magnetic flux [20, 26, 27], as a chip-based magnetic trap [19, 20] with vertical coil

^{*} witlef.wieczorek@chalmers.se

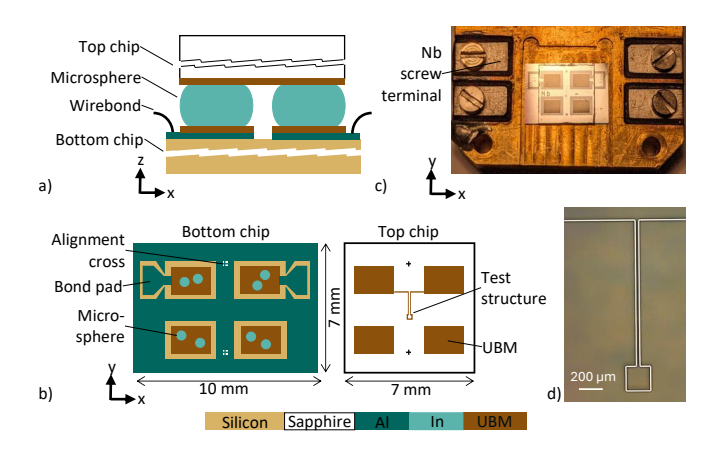


FIG. 1. Schematic representation of a flip-chip device, showing (a) the side view after assembly and (b) the top view before assembly. (c) Photograph of an assembled flip-chip wire bonded to a copper holder. (d) Optical image of a fabricated test structure on a sapphire substrate.

separation of tens of micrometers, or for transporting a supercurrent to flux-tunable couplers [28, 29].

Our paper is structured as follows. We first describe the assembly process of the flip chips via bonding through indium microspheres in a transfer stage and, for comparison, in a flip-chip bonder. We then characterize the material composition and superconducting properties of the Nb and NbN UBM thin films with and without Au passivation. Finally, we characterize the superconducting properties of assembled flip-chip devices using Nb or NbN as the UBM material and discuss the effect of oxidation and Au passivation on their performance.

II. FABRICATION AND ASSEMBLY

An overview of the flip-chip device is shown in Fig. 1. It consists of a bottom chip made from silicon and a top chip made from sapphire that allows for in situ alignment during assembly due to its transparency. The two chips are galvanically connected through indium microspheres of 300 µm diameter, which, after bonding, give a separation of below 50 µm, see Fig. 1(a). The bottom chip contains an Al wiring layer (Fig. 1(b)), which can be used, for example, to pattern a superconducting circuit. Importantly, this chip contains large areas for wire bonding to make external electrical connections to the chip. To make flip-chip interconnects, we pattern and deposit UBM pads on top of the Al layer, upon which we place indium microspheres that connect galvanically to the top chip. The top chip (Fig. 1(b)) consists of a superconducting layer, which can, for example, be shaped as a coil (see Fig. 1(d)) or other geometry. A completed flip-chip device is shown in Fig. 1(c). The fabrication process of Al, Au, Nb, and NbN thin films is described in detail in Suppl. Mat. S1.

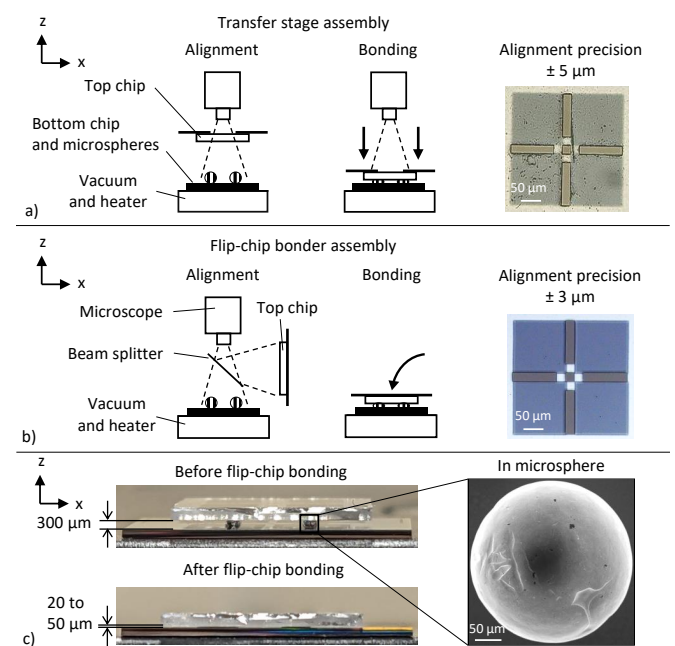


FIG. 2. Schematic of the flip-chip assembly method and picture of the alignment crosses after successful bonding for (a) the transfer stage and (b) the flip-chip bonder. (c) Flip-chip before and after bonding. The close-up is an SEM image of an indium microsphere used for flip-chip bonding.

A. Flip-chip bonding

We assembled our flip-chips using two different methods: an in-house-built transfer stage (Fig. 2(a)) and a commercial flip-chip bonder (Fig. 2(b)). The former is commonly used for the transfer of two-dimensional materials [18]. Both tools create a mechanically sturdy bond with a lateral alignment accuracy of a few micrometers. To make a galvanic and robust connection between the chips, we use commercially available 99.99 % pure indium microspheres (Fig. 2(c) right panel) [17]. The microspheres have a diameter of $300 \pm 5 \,\mu\mathrm{m}$ and a spheroid tolerance of $1.5 \,\%$. Although In possesses a native oxide, it normally passivates at a few nanometers [30]. This oxide layer is easily broken during bonding, as In is malleable and deforms significantly when pressed.

In our first approach to flip-chip bonding (Fig. 2(a)), we use an xyz micro-manipulator stage. The bottom chip is held via vacuum, and the indium microspheres are placed on the UBM pads with tweezers. We typically use two microspheres per pad. The top chip is attached to the glass slide with polydimethylsiloxane (PDMS) tape and is positioned above the bottom chip. After aligning the two chips under a microscope using alignment markers, the bottom chip can be heated to $110\,^{\circ}\mathrm{C}$ if reflow of indium is desired; otherwise, it can be kept at room temperature. The reflow temperature must remain well below $156\,^{\circ}\mathrm{C}$ to avoid melting of indium, and also low enough to prevent oxide growth that can hinder galvanic

contact with the UBM layers [30]. Finally, the top chip is brought down and pressed against the indium microspheres using the manipulator stage. Since the applied force is unknown, the pressing is stopped if any relative lateral motion between the two chips is observed. Additionally, the x-y alignment is continuously monitored and corrected during the bonding procedure.

We have also used a commercial flip-chip bonder (Fine-placer 96 Lambda from Finetech GmbH), Fig. 2(b), to bond the chips and compare performance with the manual transfer stage. The top chip is held with a vacuum on a pick-up tool that stands vertically next to the bottom chip. A beam splitter in the optical path enables both chips to be seen simultaneously. Once alignment is achieved, the microscope is retracted, and a precalibrated lever presses the top chip onto the bottom chip with a calibrated force (bonding pressure) between 50 to 65 N (60 to 80 MPa) at room temperature for a total of four microspheres pressed to approximately 500 µm diameter. The alignment cannot be monitored and corrected during bonding.

In general, the transfer stage achieved alignment accuracy (5 $\mu m)$ similar to that of the flip-chip bonder (3 $\mu m)$. However, the flip-chip bonder achieved a closer chip separation (20 $\mu m)$ compared to the transfer stage (50 $\mu m)$. The chip separation can be reduced in future devices using smaller indium microspheres. In addition, an average tilt of 2 to 3 mrad was obtained with both methods.

III. CHARACTERIZATION OF SUPERCONDUCTING UBM THIN FILMS

A. SIMS analysis of UBM thin films

We characterized the material composition of the UBM thin films using time-of-flight secondary ion mass spectrometry (TOF SIMS). Fig. 3 presents TOF SIMS depth profiles of 50 nm thin UBM films, in case of Nb/Au, NbN, and NbN/Au sputtered on the Al layer of the bottom chips, and in the case of Nb sputtered directly on the sapphire substrate of the top chips (see Fig. 1 (b)). The films were analyzed a few weeks after exposure to air. The measurement was performed using Cs⁺ primary ions with an energy of 1 keV rastered over a $50 \,\mu m \times 50 \,\mu m$ area. The Cs⁺ ions sputter the material at varying rates depending on their ion mass and ionization potential. The resulting secondary ions and their intensities were then measured by the SIMS analyzer, recording counts as a function of sputtering time. The obtained SIMS data allows us to make qualitative statements about the material composition of the films.

Fig. 3(a)-(d) show full-depth profiles until the Al layer or the sapphire substrate was reached. Fig. 3(e)-(h) show higher-resolution measurements focused on the surface region of the thin films, obtained at a separate location from the full-depth measurement and terminated when either the passivation or oxide layer signal decreased by

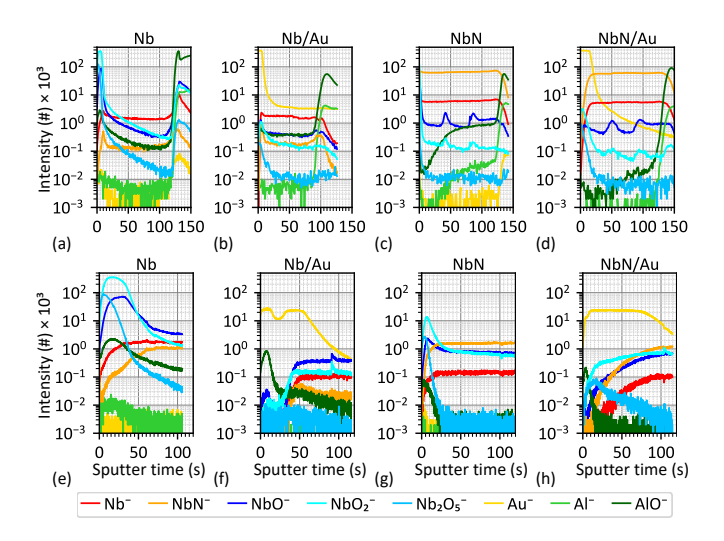


FIG. 3. TOF-SIMS depth profiles of Nb, Nb/Au, NbN, and NbN/Au thin films using Cs⁺ primary ions. (a)–(d) Full-depth profiles acquired with 1s intervals. (e)–(h) High-resolution surface profiles obtained with 0.13s intervals. The plots show secondary ion intensity as a function of sputtering time for key elements and compounds present in the samples.

approximately an order of magnitude.

Non-passivated Nb and NbN films (Fig. 3a,c,e,g) exhibit dominant native oxides (NbO, NbO₂, Nb₂O₅) in the surface region, rapidly decreasing in the bulk region. In contrast, Au-passivated films (Fig. 3b,d,f,h) show strong Au signals at the surface with minimal oxide presence, demonstrating effective passivation. The underlying Nb or NbN layers in all samples demonstrate stable signals throughout the respective UBM film thickness. A sharp increase in the Al and AlO signals marks the UBM/Al interface for the Nb/Au, NbN, and NbN/Au thin films and the UBM/sapphire interface for the Nb thin film.

B. Superconducting properties of UBM thin films

We deposited the UBM layer on separate chips and patterned a test structure to determine the transition temperature T_c and the critical current I_c of the UBM thin film. The test structure is a narrow coil that is 10 µm wide and 4740 µm long patterned on a 50 nm thick UBM layer (see Fig. 1(d)).

All measurements were performed inside a dilution refrigerator, allowing us to characterize samples down to millikelvin temperature. The chips are glued with BF-6 glue to a copper sample holder, as shown in Fig. 1(c). The test structure bond pads are connected to Nb screw terminals on a sample holder with Al wirebonds (25 µm diameter). Below the T_c of Al, each Al bond wire can carry a supercurrent of up to 85 mA. The screw terminals are used to clamp twisted niobium-titanium (Nb-Ti) wires that are soldered to a DC breakout on the 4 K plate of the cryostat. Thus, the entire line is superconducting below the 4 K plate. Electrical characterization

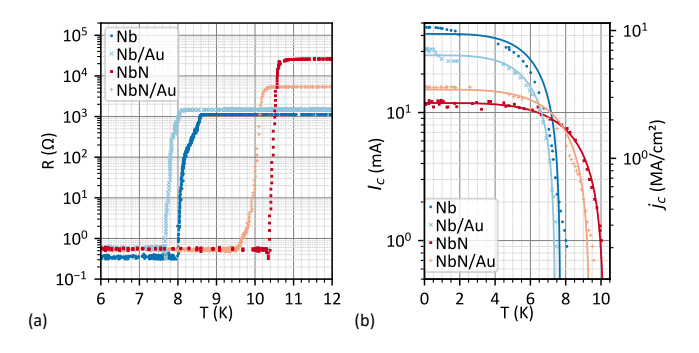


FIG. 4. Measurements of superconducting thin films. (a) Resistance as a function of temperature at $10 \,\mu\text{A}$ bias current. Note that the measured resistance below T_c is due to the input voltage offset of the voltmeter with $10 \,\mu\text{A}$ bias current. (b) Critical current and critical current density as a function of temperature. The solid line is a fit using Eq. 1.

is performed by measuring the resistance of a four-wire connection to the device under test, which excludes the wire bonds and other connections to the sample. The bias current is provided with a Keithley 2450 source, and voltage is measured by a Rohde & Schwarz HMC8012. The contribution of the Al bond pads to the resistance and the critical current is negligible due to their large cross-sectional area (1 mm \times 150 nm) and surface sheath area (determined by $\lambda_L=54\,\mathrm{nm}$ [31]) compared to the test structure. We therefore calculate the critical current density j_c of the thin films considering the relevant geometric feature size of the superconductor and bulk transport for type II superconductors, Nb and NbN, and screening transport for type I superconductors, Al and In.

Fig. 4(a) shows the resistance R of the test structure as a function of temperature, measured with a bias current of 10 µA. The thin films exhibit a normal-state resistance above T_c , which is in accordance with literature; see Suppl. Mat. S2. A sharp transition in resistance is observed at the respective T_c (taken as the temperature at which the resistance is at least tenfold the residual resistance), indicating the onset of superconductivity. The respective T_c for the Nb and NbN thin film is 8.0 K and 10.4 K, respectively, similar to the values reported in Refs. [32, 33]. The T_c of our Nb film is lower than the commonly reported value of 9 K. We believe that this could be due to disorder in our film [34], the presence of native oxides [35] (see Fig. 3(e)), or geometric constrictions [32] in our test structure. The Au-passivated thin films show a T_c for Nb/Au and NbN/Au of 7.7 K and 9.8 K, respectively, slightly lower than their nonpassivated counterparts. We attribute this small reduction in T_c to the proximity effect [36] induced by the Au capping layer on Nb [37] or NbN [38].

Fig. 4(b) shows the dependence of the thin film's critical current on the sample's temperature. We infer the I_c at each temperature from individual measurements, in which we increase the current in steps of $0.1 \,\mu\text{A}$ until the

Thin film material [thickness]	$j_c \ (\mathrm{MA/cm^2})$		T_c (K)	
	Exp.	Lit.	Exp.	Lit.
Nb[50 nm]	9.3	4 [32]	8.0	8.1 [32]
Nb[50 nm] / Au[5 nm]	6.3	-	7.7	7.3 [37]
$NbN[50\mathrm{nm}]$	2.5	2.5 [39]	10.4	10.6 [33]
$\frac{\text{NbN[50 nm]} / \text{Au[5 nm]}}{\text{NbN[50 nm]}} = \frac{\text{NbN[50 nm]}}{NbN[5$	3.2	-	9.9	10.2 [38]

TABLE I. Superconducting properties of the sputtered UBM layers patterned independently on a sapphire substrate. The literature values are taken from works that use similar deposition techniques and film thicknesses.

4-wire voltage increases sharply by a factor of 10 as a result of the transition from superconducting to normal conducting state. An increase in the temperature of the cryostat accompanies this increase in resistance. Hence, before taking the next measurement, we wait a sufficient amount of time for the cryostat to thermalize to the desired temperature. From the data shown in Fig. 4(b), we obtain a similar T_c as in the resistance measurements (Fig. 4(a)). At temperatures approaching T_c , I_c drops drastically, as expected. We fit the data assuming the simple two-fluid model [40] as $(t = T/T_c)$:

$$I_c = I_{c0} \left(1 - t^4 \right).$$
 (1)

This fit agrees well with the data, as seen in Fig. 4(b). At base temperature ($\sim 100\,\mathrm{mK}$), we determine j_c of the thin films to be $9.26\,\mathrm{MA\,cm^{-2}}$ and $2.5\,\mathrm{MA\,cm^{-2}}$ for Nb and NbN, respectively, similar to other works; see Tab. I. The j_c of Nb/Au ($6.3\,\mathrm{MA\,cm^{-2}}$) and NbN/Au ($3.2\,\mathrm{MA\,cm^{-2}}$) are close to their non-passivated counterparts.

IV. SUPERCONDUCTING FLIP-CHIP DEVICES

The flip-chip devices that we patterned with NbN, NbN/Au, or Nb/Au as the UBM layer were fully superconducting at millikelvin temperatures (Fig. 5 (a)) and thus are useful devices for making superconducting flip-chip-based interconnects. In contrast, the non-passivated Nb-based flip chip showed a finite resistance of some tens of ohm at millikelvin temperatures, which we attribute to the presence of the native oxide layer on top of Nb (see Fig. 3(e)). Thus, in the following, we will focus on discussing the functioning NbN, NbN/Au, and Nb/Au-based flip-chip devices.

Fig. 5(a) shows the temperature dependence of the resistance of the superconducting flip-chip devices. We observe resistance transitions at the T_c of the respective superconducting materials. At 1.25 K, all three flip-chip devices show a sharp increase in resistance, which marks the T_c of Al. We estimate a normal-state resistivity of Al

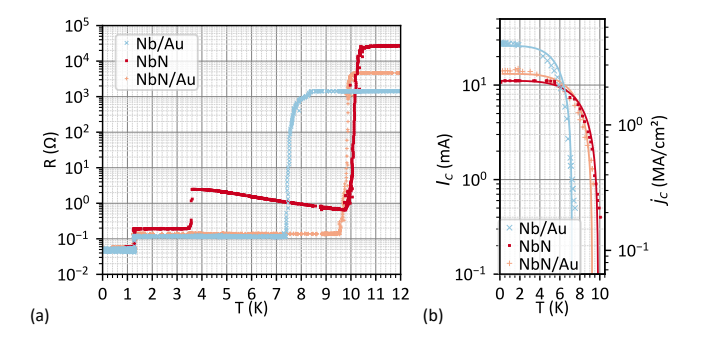


FIG. 5. Measurements of flip-chip devices. (a) Resistance as a function of temperature at $100\,\mu\mathrm{A}$ bias current. Note that the measured resistance of $0.06\,\Omega$ at temperatures below $1.25\,\mathrm{K}$ is limited by the measurement setup. (b) Critical current and critical current density as a function of temperature.

to be between $0.68\,\mu\Omega\cdot\mathrm{cm}$ and $1.6\,\mu\Omega\cdot\mathrm{cm}$, which is comparable to that reported in Ref. [41]. The resistance of flip-chip devices that use Au-passivated UBM layers remains constant between the T_c of Al and another sharp transition in resistance at $7.4\,\mathrm{K}$ for the Nb/Au and $10.0\,\mathrm{K}$ for the NbN/Au flip-chip device (see Tab. II), respectively. These temperatures mark the respective T_c of the utilized UBM thin films and are similar to those determined for the thin films only (Tab. I). Above their respective T_c , all flip-chip devices exhibit resistance values (Tab. S2) corresponding to their normal-state resistances, as observed for their respective thin films (Tab. S1).

The non-passivated NbN flip-chip device shows an additional sharp increase in resistance at 3.5 K, which corresponds to the T_c of In. Given the geometry of our In microspheres, we estimate their normal-state resistance to be some $n\Omega$, which is well below the observed resistance change. Instead, we attribute the finite resistance to the thin native oxide layer that forms on the surface of the non-passivated NbN film due to exposure to air. Fig. 3(c),(g) show the presence of the NbO_x oxides NbO, NbO₂, and Nb₂O₅ in the non-passivated NbN film. In contrast, oxide growth is effectively prevented in the Aupassivated NbN thin film (see Fig. 3(d),(h)). We assume that the NbO_x oxide layer acts as an insulator and estimate its resistivity to be of the order of $10^6 \,\Omega \cdot \mathrm{cm}$ (see Suppl. Mat. S2), which is reasonable for NbO₂ oxide[42]. NbO_2 was also identified in Ref. [43] as a relevant oxide of superconducting NbN thin films. Then, below the T_c of In, the NbN/NbO $_x$ /In interface forms a superconductorinsulator-superconductor (SIS) connection and, thus, can transport a superconducting current below the critical current of the SIS connection. We estimate this critical current to be around 2 mA (see Suppl. Mat. S3 A). Close to this value, we also observe a finite resistance step in a current-dependent measurement of the NbN flip-chip device (see Suppl. Mat. S3B). The passivated NbN flipchip device does not show this behavior, and therefore, we recommend that the passivation of the utilized UBM materials be used in galvanic contacts.

Fig. 5(b) shows the temperature dependence of the flip-chip's critical current. The critical current behavior of the flip-chip devices is governed by the smallest superconducting structure on the flip chip, which in our case was the test structure on the top chip's UBM layer (see Fig. 1(d)). The data is well described by Eq. 1, and the observed T_c values agree well with those determined from the data of Fig. 5(a). The flip-chip devices exhibit slightly lower T_c (see Tab. II) than their thin-film counterparts (see Tab. I), which we attribute to the proximity effect from the Al layer [44] below the respective UBM layer on each bottom chip. We infer a maximum I_c (j_c) at ~100 mK of 28 mA (5.6 MA cm⁻²) and 15 mA $(3.0\,\mathrm{MA\,cm^{-2}})$ for the Nb/Au and NbN/Au flip-chip devices, respectively, which are similar to their thin-film counterparts (see Tab. I).

Importantly, we also determined the I_c of the indium microsphere-based interconnects (for details, see Suppl. Mat. S4). To this end, we assembled a simplified flip-chip device (see Fig. S3(b)) using three unpatterned chips of Nb/Au film chosen for its high critical current and absence of oxidation. Two In microspheres were placed on each bottom chip, while a third chip was pressed on top to establish a galvanic connection between the two bottom chips. We used 24 aluminum wire bonds per bond pad to allow the transport of large supercurrents. With this flip-chip device, we could run a supercurrent of up to 2 A (see Suppl. Mat. S4), limited by the maximum output of the current source.

UBM material [thickness]	j_c (MA/cm ²)	T_c (K)
Nb[50 nm] / Au[5 nm]	5.6	7.4
NbN[50 nm]	0.4^{*}	10.0
$\frac{\text{NbN}[50\text{nm}]}{\text{Au}[5\text{nm}]}$	3.0	9.7

TABLE II. Superconducting properties of the flip-chip devices with different UBM materials. *The NbN flip-chip exhibits $2.2\,\mathrm{MA/cm^2}$ limited by the NbN test structure, and $0.4\,\mathrm{MA/cm^2}$ limited by Nb oxide in the interconnect.

V. CONCLUSION AND OUTLOOK

We have presented a novel approach for superconducting flip-chip devices using 300 μm diameter In microspheres for bonding on Au-passivated Nb- or NbN-based UBM layers. Our assembly method achieves chip separations of 20 to 50 μm with a transversal alignment accuracy of better than 5 μm and a tilt of 2 to 3 mrad using either a transfer stage or a conventional flip-chip bonder. Smaller chip separations can be achieved using smaller indium microspheres.

Our flip-chip assembly is suitable for high-current applications. The $300\,\mu\mathrm{m}$ indium interconnects themselves can carry currents exceeding 1 A at millikelvin temperatures. With patterned superconducting thin films, we

have demonstrated that our flip-chip devices could run tens of mA at temperatures below the superconducting transition of Al, which was used as a wiring layer in the bottom chip. We investigated the impact of oxidation on the UBM thin films, finding that although native oxides were present in both Nb and NbN flip-chips, only the latter were superconducting at millikelyin temperatures. An Au passivation layer enabled functioning Nb flip-chip devices, opening up the possibility for high-current applications since the critical current density of Nb is larger than that of NbN or Al.

The presented flip-chip devices are suitable for various superconducting devices, such as chip-based high-current magnetic traps [19, 20] or solenoids [21], efficient flux readout in SQUID-based sensors [20, 27], or transport of supercurrent to flux-tunable superconducting couplers [28, 29]. Thus, our flip-chip devices can find applications in superconducting-based sensors [6, 7] or quantum technologies [1–5, 27].

ACKNOWLEDGMENTS

The authors thank Marcus Rommel and Henrik Frederiksen for their support in microfabrication, Hanlin Fang and Thilo Bauch for technical support, and Per Malmberg for TOF-SIMS measurements. This work was supported in part by the Horizon Europe 2021-2027 framework program of the European Union under Grant Agreement No. 101080143 (SuperMeQ), the European Research Council under Grant No. 101087847 (ERC Consolidator SuperQLev), the Knut and Alice Wallenberg (KAW) Foundation through a Wallenberg Academy Fellowship (WW), and the Wallenberg Center for Quantum Technology (WACQT, AP). The devices were fabricated at Chalmers Myfab Nanofabrication Laboratory and analyzed in part at Chalmers Materials Analysis Laboratory (CMAL).

Data availability: Data underlying the results presented in this paper are available in the open-access Zenodo database: 10.5281/zenodo.13377107.

SUPPLEMENTARY MATERIAL

S1. FABRICATION

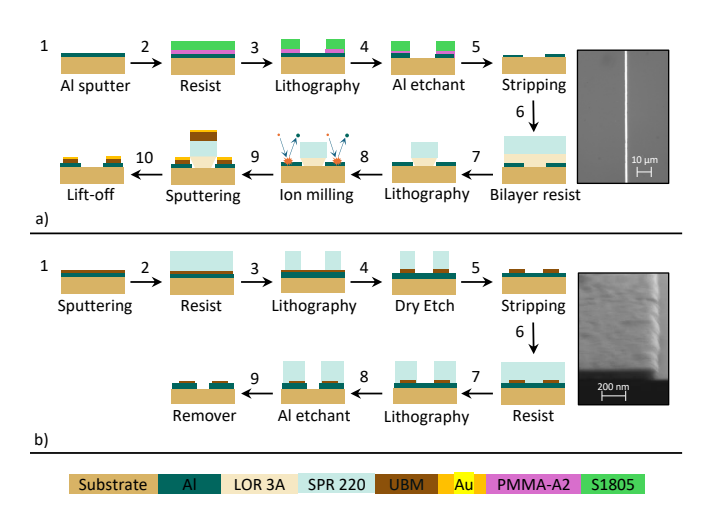


FIG. S1. (a) Schematic of the liftoff process. Right: an optical image of a $2\,\mu m$ wide test structure. (b) Schematic of the etching process. Right: SEM image of a $100\,n m$ thick UBM film.

In the following, we describe the fabrication of the layers on the bottom chip since it contains the UBM layer and the additional Al wiring layer. We present two approaches for patterning the UBM layer: a liftoff process and an etching process. The top chip consists of only the UBM layer patterned with pads and the test structure, and thus, the fabrication procedure is the same as that for the bottom chip without the process steps of the Al layer. Before any film is deposited, the wafers are cleaned in an ultrasonic bath with acetone, followed by isopropyl alcohol (IPA).

The liftoff process (Fig. S1(a)) begins with the fabrication of an Al wiring layer. First, 150 nm of Al is sputtered on a 2" Si wafer using a DC magnetron sputtering tool. The deposition is followed by spin coating of resist S1805, exposing the pattern with optical lithography and developing the resist in MF-319. The developed area is first descummed by ashing the resist residue in O₂ plasma at 40 W for 90 s. The Al layer is then etched in Transene Etchant A at 40 °C for 90 s and rinsed with water. Finally, the resist is stripped with Remover 1165, and the wafer is cleaned as mentioned above. The UBM layer is fabricated by spin-coating the wafer with a bilayer resist (LOR 3A $(0.4 \,\mu\text{m})$ & SPR 220 $(3 \,\mu\text{m})$) to create an undercut and avoid sidewall deposition for easier liftoff. The pattern is then exposed using optical lithography and developed in MF-24A. The wafer is flood-exposed using a UV lamp to prevent bubble formation during sputtering due to trapped N₂, followed by descumming in O₂ plasma as before. To deposit the UBM layer, we use a magnetron sputtering system with an Nb DC source at

a base pressure of $\sim 10^{-8}$ mbar. Before sputtering, we ion-milled the surface with an Ar flow of 2 sccm and a beam current of 10 mA for 50 s to remove native Al oxide for galvanic contact between the wiring layer and the UBM pads. The DC power source is set at 200 W during the deposition of Nb and NbN and sputtered in steps of 17 nm to avoid excessive heating and therefore bubbling of the resist during deposition. Additionally, for depositing NbN, the N₂ flow is set at 8 sccm and the Ar flow to 60 sccm for a stoichiometry of approximately 1:1. Surface profilometry shows that the thickness uniformity of the Nb or NbN film is precise to within 10 percent of the desired thickness. A thin layer of $5\,\mathrm{nm}$ Au is sputtered in the same vacuum for devices with passivation. Finally, the wafer is soaked overnight in Remover 1165 for liftoff of the UBM layer (along with the Au layer, if present) and then cleaned with acetone and IPA.

In the etching process (Fig. S1(b)), the Al wiring layer and the UBM layer (Nb or NbN) are sputtered in the same vacuum, one after the other, on a pre-cleaned bare wafer. The UBM resist mask is then patterned on top of the thin film using SPR220 and optical lithography. After the resist is developed, the wafer is placed in a reactive ion etching chamber. The UBM layer is selectively etched with NF₃ gas, which does not attack the Al layer beneath. The resist is dissolved in Remover 1165, and a second resist mask of SPR220 is patterned to define the wiring layer. After development and ashing, the wafer is submerged in a Transene etchant bath to etch the Al layer. Finally, the resist mask is dissolved in Remover 1165, and the wafer is cleaned as stated above.

Both processes are suitable alternatives for fabricating the desired material stacks. In some devices, the adhesion of Au to Nb was inadequate. Future processes could mitigate this issue by incorporating an additional 5 nm layer of Ti as an adhesion promoter [24]. With liftoff, we have reliably patterned long and narrow features with widths as small as 2 µm using optical lithography (Fig. S1(a)) and can, in principle, pattern sub-um features using e-beam lithography. Patterning such features via etching requires a high degree of control over selectivity, anisotropy, and etch rate. Therefore, the liftoff process is preferred to pattern narrow and long coil features [19, 20], coplanar waveguides [22], or microbridges [45, 46]. However, liftoff is viable only up to a certain film thickness, beyond which the resist may harden during deposition and become insoluble, or the resist may not be thick enough. Thus, an etching-based process is preferred for layers thicker than 100 nm (Fig. S1(b)). Certain deposition tools lack ion milling capability but can deposit multiple materials within the same vacuum environment. In that case, the etching process can be used to successively pattern each film with suitable selective etching processes.

S2. RESISTANCE DATA

A. UBM materials

We summarize the measured resistance R, the calculated resistivity ρ (both determined at 12 K and 300 K), and the calculated residual resistance ratio $RRR = R_{300\,\mathrm{K}}/R_{12\,\mathrm{K}}$ for the UBM thin films in Tab. S1 and for the flip-chip devices in Tab. S2.

The $\rho_{300\,\mathrm{K}}$ and RRR of the non-passivated thin films align with Refs. [22, 47]. The Au-passivated films exhibit lower $\rho_{300\,\mathrm{K}}$ values compared to their non-passivated counterparts due to the parallel resistance of the Au layer.

To verify the effect of the Au film, we estimate $\rho_{300\,\mathrm{K}}$ of 5 nm Au to be $11\,\mu\Omega\cdot\mathrm{cm}$ [48], and obtain $\rho_{300\,\mathrm{K}}$ of $15\,\mu\Omega\cdot\mathrm{cm}$ for Nb and $69\,\mu\Omega\cdot\mathrm{cm}$ for NbN, close to our measured values. Similarly, using $\rho_{12\,\mathrm{K}}$ of Au to be $2.6\,\mu\Omega\cdot\mathrm{cm}$ [49], we calculate $\rho_{12\,\mathrm{K}}$ of $9\,\mu\Omega\cdot\mathrm{cm}$ for Nb and $26\,\mu\Omega\cdot\mathrm{cm}$ for NbN.

The corresponding values of the flip-chip devices are very close to those of their thin-film counterparts, with slightly lower R, and therefore ρ , due to the parallel resistance of the Si substrate.

B. Aluminum thin film

The resistance of the Al film is obtained from the resistance step observed at the T_c of Al (Fig. 5(a)) to be about 0.08 to 0.2 Ω . Considering the smallest cross-sectional area in the Al layer (300 µm \times 150 nm of length 400 µm), we estimate that the normal-state resistivity of Al lies between 0.68 µ Ω · cm and 1.6 µ Ω · cm, which is comparable to that reported in Ref. [50].

C. Indium microsphere

Bulk indium exhibits an electrical resistivity of $1.2\,\mathrm{n}\Omega\cdot\mathrm{cm}$ at 4 K [51]. Approximating a pressed indium microsphere as a cylinder with 500 µm diameter and 50 µm height yields an estimated normal-state resistance of $30\,\mathrm{n}\Omega$.

S3. NON-PASSIVATED NBN FLIP-CHIP

A. Critical current of the SIS junction

In the non-passivated NbN flip-chip device, we observe a resistance step of $2.5\,\Omega$ at the transition temperature of In (see Fig. 5(a)). We assume that this resistance comes from the oxide on top of NbN. Considering a contact area with a diameter of about 500 µm (for pressed microspheres) and an oxide thickness of $0.5\,\mathrm{nm}$ (estimated from the SIMS data, Fig. 3(g), assuming a sputtering

rate of $3.6 \,\mathrm{nm/min}$ [52]) we obtain a resistivity of the order of $10^6 \,\Omega \cdot \mathrm{cm}$, which is expected for NbO₂ at such low temperatures [42].

The total resistance $R=2.5\,\Omega$ is assumed to be evenly distributed at each oxide interface of the entire flip-chip. Since the In microsphere is pressed with NbN on top and bottom, we consider two oxide interfaces in series per microsphere. Considering two microspheres per pad implies that the normal-state resistance at each interface is $R_N=R/2=1.25\,\Omega$.

Using the Ambegaonkar-Baratoff equation [40], we can then estimate the critical current of the SIS junction formed by the $NbN/NbO_x/In$ interface as

$$I_{c0} = \frac{\pi \sqrt{\Delta_{In} \Delta_{NbN}}}{2eR_N} \tanh\left(\frac{\sqrt{\Delta_{In} \Delta_{NbN}}}{2k_B T}\right), \quad (S1)$$

where $k_{\rm B}$ is Boltzmann's constant, e electric charge, T temperature (100 mK), the superconducting energy gaps of NbN $\Delta_{NbN} = 4.16 \,\mathrm{meV}$ [53] and In $\Delta_{In} = 1.05 \,\mathrm{meV}$ [54]. We obtain $I_{c0} = 2.6 \,\mathrm{mA}$.

B. Current measurement

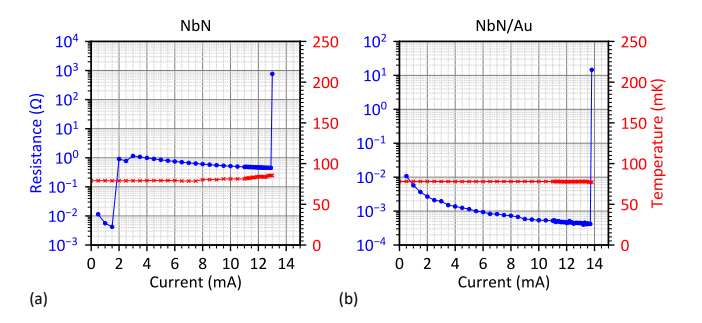


FIG. S2. Current-dependent measurements of (a) non-passivated NbN and (b) Au-passivated NbN flip chip devices. The plots show resistance (blue circles) and temperature at the MXC stage (red crosses) as a function of current. Lines are a guide to the eye.

Fig. S2 shows resistance vs. current measurements of the non-passivated NbN and Au-passivated NbN flip-chip devices. For both flip-chip devices, we observe a sharp increase in resistance above a current of $12\,\mathrm{mA}$, which indicates the critical current through the test structure of the NbN thin film. For the non-passivated NbN flip-chip device (Fig. S2(a)), we observe an additional resistance step of about $1\,\Omega$ starting at a current close to $2\,\mathrm{mA}$. We attribute this additional resistance step to the presence of the interface oxide in the flip-chip interconnect, which forms an SIS junction with about this critical current, which is close to the estimated $2.6\,\mathrm{mA}$ from the Ambegaonkar-Baratoff equation.

Thin film material [thickness]	$R_{12 \mathrm{K}} \ (\mathrm{k}\Omega)$	$R_{300 \mathrm{K}} \ (\mathrm{k}\Omega)$	$\rho_{12 \mathrm{K}} \ (\mu\Omega \cdot \mathrm{cm}) \ (\mu\Omega \cdot \mathrm{m})$		$ ho_{300\mathrm{K}} \ \Omega\cdot\mathrm{cm})$	RRR	
				Exp.	Lit.	Exp.	Lit.
Nb[50 nm]	1.13	2.89	11.9	30.5	19.4 [22]	2.6	6.5 [22]
Nb[50 nm] / Au[5 nm]	1.47	2.54	17.1	29.5	-	1.73	-
$NbN[50\mathrm{nm}]$	26.1	21.9	278	233	$\sim 250 \ [47]$	0.84	$\sim 0.8 [47]$
$\frac{\text{NbN}[50\text{nm}]}{\text{NbN}[50\text{nm}]} / \text{Au}[5\text{nm}]$	5.41	6.50	62.9	75.6		1.2	

TABLE S1. Electrical properties of the sputtered UBM layers patterned independently on a sapphire substrate. The literature values are taken from works that use similar deposition techniques and film thicknesses.

UBM material [thickness]	$R_{12 \mathrm{K}} \ \mathrm{(k\Omega)}$	$R_{300 \mathrm{K}} \ \mathrm{(k\Omega)}$	$\begin{array}{c} \rho_{12\mathrm{K}} \\ (\mu\Omega\cdot\mathrm{cm}) \end{array}$	$ ho_{300\mathrm{K}}\ (\mu\Omega\cdot\mathrm{cm})$	RRR
Nb[50 nm] / Au[5 nm]	1.42	2.66	16.52	30.86	1.87
NbN[50 nm]	27.2	21.7	286.7	228.9	0.81
NbN[50 nm] / Au[5 nm]	4.69	5.80	54.5	67.3	1.23

TABLE S2. Electrical properties of the flip-chip devices with different UBM materials.

S4. CRITICAL CURRENT OF IN MICROSPHERE

The critical current of two Indium microspheres is measured to be above 2 A (see Fig. S3(a)). In our measurement, we were limited by the maximum output of our current source, which was 2 A. Assuming a diameter (d) of the contact area of the pressed In microsphere of 500 µm and the current in this type I superconductor to be flowing only within the London penetration depth of $40 \,\mathrm{nm}$ [55] we estimate the j_c of In to be greater than $1.6 \,\mathrm{MA/cm^2}$. Considering a critical field (H_c) of 2.75×10^{-2} T [56] for pure bulk In, we estimate the critical current (I_c) using the Silsbee criterion $(I_c = \pi dH_c \ [40])$ to be about 34 A, which is higher than the value we can measure with the available current source. The observed heating in the fridge for currents larger than about 1.2 A is the result of Joule heating at the 4K stage, where the superconducting NbTi connection terminates in a normal copper connection. During measurement, this connection heats up, which is seen as a rise in temperature at the 4K stage in Fig. S3. This heat propagates down to the sample, which is seen as a rise in the base temperature at the MXC stage.

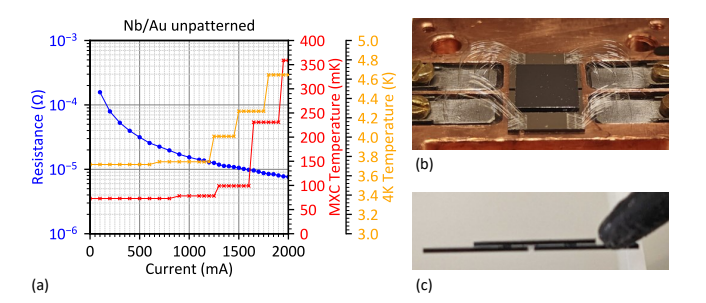


FIG. S3. (a) Current measurement of an unpatterned Nb/Au flip chip using In microsphere interconnects. The plot shows resistance (blue curve) as well as temperature at the mK stage (red curve) and 4K stage (orange curve) in dependence of current. Image of (b) the assembled Nb/Au flip chip and (c) a close-up of its cross-section. The flip chip was wire bonded with 24 Al bonds per pad.

- B. Foxen, J. Y. Mutus, E. Lucero, R. Graff, A. Megrant, Y. Chen, C. Quintana, B. Burkett, J. Kelly, E. Jeffrey, and et al., Qubit compatible superconducting interconnects, Quantum Science and Technology 3, 014005 (2017).
- [2] D. Rosenberg, D. Kim, R. Das, D. Yost, S. Gustavsson, D. Hover, P. Krantz, A. Melville, L. Racz, G. O. Samach, and et al., 3d integrated superconducting qubits, npj Quantum Information 3, 10.1038/s41534-017-0044-0 (2017).
- [3] C. R. Conner, A. Bienfait, H.-S. Chang, M.-H. Chou, Dumur, J. Grebel, G. A. Peairs, R. G. Povey, H. Yan, Y. P. Zhong, and et al., Superconducting qubits in a flip-chip architecture, Applied Physics Letters 118, 10.1063/5.0050173 (2021).
- [4] S. Kosen, H.-X. Li, M. Rommel, D. Shiri, C. Warren, L. Grönberg, J. Salonen, T. Abad, J. Biznárová, M. Caputo, and et al., Building blocks of a flip-chip integrated superconducting quantum processor, Quantum Science and Technology 7, 035018 (2022).
- [5] G. J. Norris, L. Michaud, D. Pahl, M. Kerschbaum, C. Eichler, J.-C. Besse, and A. Wallraff, Improved parameter targeting in 3d-integrated superconducting circuits through a polymer spacer process, EPJ Quantum Technology 11, 10.1140/epjqt/s40507-023-00213-x (2024).
- [6] N. S. DeNigris, J. A. Chervenak, S. R. Bandler, M. P. Chang, N. P. Costen, M. E. Eckart, J. Y. Ha, C. A. Kilbourne, and S. J. Smith, Fabrication of flexible superconducting wiring with high current-carrying capacity indium interconnects, Journal of Low Temperature Physics 193, 687–694 (2018).
- [7] T. J. Lucas, J. P. Biesecker, W. B. Doriese, S. M. Duff, G. C. Hilton, J. N. Ullom, M. R. Vissers, and D. R. Schmidt, Indium bump process for low-temperature detectors and readout, Journal of Low Temperature Physics 209, 293–298 (2022).
- [8] M. Plötner, G. Sadowski, S. Rzepka, and G. Blasek, Aspects of indium solder bumping and indium bump bonding useful for assembling cooled mosaic sensors, Microelectronics International 8, 27–30 (1991).
- [9] Q. Huang, G. Xu, Y. Yuan, X. Cheng, and L. Luo, Development of indium bumping technology through az 9260 resist electroplating, Journal of Micromechanics and Microengineering 20, 055035 (2010).
- [10] K. Wade and A. Banister, The Chemistry of Aluminium, Gallium, Indium and Thallium, 1st ed., Pergamon Texts in Inorganic Chemistry, Vol. 12 (Pergamon Press, Oxford, UK, 1973) p. 107.
- [11] R. G. Gordon, X. Liu, R. N. Broomhall-Dillard, and Y. Shi, Highly conformal diffusion barriers of amorphous niobium nitride, MRS Proceedings 564, 10.1557/proc-564-335 (1999).
- [12] C. Thomas, J.-P. Michel, E. Deschaseaux, J. Charbonnier, R. Souil, E. Vermande, A. Campo, T. Farjot, G. Rodriguez, G. Romano, and et al., Superconducting routing platform for large-scale integration of quantum technologies, Materials for Quantum Technology 2, 035001 (2022).
- [13] M. Volpert, L. Roulet, J.-F. Boronat, I. Borel, S. Pocas, and H. Ribot, Indium deposition processes for ultra fine pitch 3d interconnections, 2010 Proceedings 60th Elec-

- tronic Components and Technology Conference (ECTC) , 1739 (2010).
- [14] P. Kozłowski, K. Czuba, K. Chmielewski, J. Ratajczak, J. Branas, A. Korczyc, K. Regiński, and A. Jasik, Indium-based micro-bump array fabrication technology with added pre-reflow wet etching and annealing, Materials 14, 6269 (2021).
- [15] R. Das, V. Bolkhovsky, C. Galbraith, D. Oates, J. Plant, R. Lambert, S. Zarr, R. Rastogi, D. Shapiro, M. Docanto, T. Weir, and L. Johnson, Interconnect scheme for die-todie and die-to-wafer-level heterogeneous integration for high-performance computing, in 2019 IEEE 69th Electronic Components and Technology Conference (ECTC) (2019) pp. 1611–1621.
- [16] K. J. Satzinger, C. R. Conner, A. Bienfait, H.-S. Chang, M.-H. Chou, A. Y. Cleland, Dumur, J. Grebel, G. A. Peairs, R. G. Povey, and et al., Simple non-galvanic flipchip integration method for hybrid quantum systems, Applied Physics Letters 114, 10.1063/1.5089888 (2019).
- [17] CAPLINQ, In100 pure indium solder spheres.
- [18] Q. Zhao, T. Wang, Y. K. Ryu, R. Frisenda, and A. Castellanos-Gomez, An inexpensive system for the deterministic transfer of 2d materials, Journal of Physics: Materials 3, 016001 (2020).
- [19] M. G. Latorre, A. Paradkar, D. Hambraeus, G. Higgins, and W. Wieczorek, A chip-based superconducting magnetic trap for levitating superconducting microparticles, IEEE Transactions on Applied Superconductivity 32, 1 (2022).
- [20] M. G. Latorre, G. Higgins, A. Paradkar, T. Bauch, and W. Wieczorek, Superconducting microsphere magnetically levitated in an anharmonic potential with integrated magnetic readout, Phys. Rev. Appl. 19, 054047 (2023).
- [21] A. L. Graninger, M. R. Longo, M. Rennie, R. Shiskowski, K. Mercurio, M. Lilly, and C. H. Smith, Superconducting on-chip solenoid for josephson junction characterization, Applied Physics Letters 115, 10.1063/1.5110170 (2019).
- [22] J. Verjauw, A. Potocnik, M. Mongillo, R. Acharya, F. Mohiyaddin, G. Simion, A. Pacco, T. Ivanov, D. Wan, A. Vanleenhove, L. Souriau, J. Jussot, A. Thiam, J. Swerts, X. Piao, S. Couet, M. Heyns, B. Govoreanu, and I. Radu, Investigation of microwave loss induced by oxide regrowth in high-q niobium resonators, Phys. Rev. Appl. 16, 014018 (2021).
- [23] M. V. P. Altoé, A. Banerjee, C. Berk, A. Hajr, A. Schwartzberg, C. Song, M. Alghadeer, S. Aloni, M. J. Elowson, J. M. Kreikebaum, E. K. Wong, S. M. Griffin, S. Rao, A. Weber-Bargioni, A. M. Minor, D. I. Santiago, S. Cabrini, I. Siddiqi, and D. F. Ogletree, Localization and mitigation of loss in niobium superconducting circuits, PRX Quantum 3, 020312 (2022).
- [24] R. N. Das, J. Yoder, D. Rosenberg, D. Kim, D. Yost, J. Mallek, D. Hover, V. Bolkhovsky, A. Kerman, and W. Oliver, Cryogenic qubit integration for quantum computing, in 2018 IEEE 68th Electronic Components and Technology Conference (ECTC) (2018) pp. 504-514.
- [25] D. Hamilton, C. Raub, B. Matthias, E. Corenzwit, and G. Hull, Some new superconducting compounds, Journal of Physics and Chemistry of Solids 26, 665–667 (1965).

- [26] M. G. Latorre, J. Hofer, M. Rudolph, and W. Wieczorek, Chip-based superconducting traps for levitation of micrometer-sized particles in the meissner state, Superconductor Science and Technology 33, 105002 (2020).
- [27] P. Schmidt, R. Claessen, G. Higgins, J. Hofer, J. J. Hansen, P. Asenbaum, M. Zemlicka, K. Uhl, R. Kleiner, R. Gross, H. Huebl, M. Trupke, and M. Aspelmeyer, Remote sensing of a levitated superconductor with a fluxtunable microwave cavity, Phys. Rev. Appl. 22, 014078 (2024).
- [28] Y. Chen, C. Neill, P. Roushan, N. Leung, M. Fang, R. Barends, J. Kelly, B. Campbell, Z. Chen, B. Chiaro, and et al., Qubit architecture with high coherence and fast tunable coupling, Physical Review Letters 113, 10.1103/physrevlett.113.220502 (2014).
- [29] Z. Niu, W. Gao, X. He, Y. Wang, Z. Wang, and Z.-R. Lin, Dc flux crosstalk reduction with dual flux line, Applied Physics Letters 124, 10.1063/5.0208859 (2024).
- [30] H. Schoeller and J. Cho, Oxidation and reduction behavior of pure indium, Journal of Materials Research 24, 386–393 (2009).
- [31] D. López-Núñez, Q. P. Montserrat, G. Rius, E. Bertoldo, A. Torras-Coloma, M. Martínez, and P. Forn-Díaz, Magnetic penetration depth of aluminum thin films (2023), 2311.14119 [cond-mat.supr-con].
- [32] Y. W. Kim, Y. H. Kahng, J.-H. Choi, and S.-G. Lee, Critical properties of submicrometer-patterned nb thin film, IEEE Transactions on Applied Superconductivity 19, 2649 (2009).
- [33] D. Niepce, Superinductance and fluctuating two-level systems loss and noise in disordered and non-disordered superconducting quantum devices, Ph.D. thesis, Chalmers University of Technology (2020).
- [34] T. Freitas, J. Gonzalez, V. Nascimento, A. Takeuchi, and E. Passamani, Negative magnetoresistance in sputtered niobium thin films grown on silicon substrates, Current Applied Physics 17, 1532–1538 (2017).
- [35] M. David Henry, S. Wolfley, T. Monson, B. G. Clark, E. Shaner, and R. Jarecki, Stress dependent oxidation of sputtered niobium and effects on superconductivity, Journal of Applied Physics 115, 10.1063/1.4866554 (2014).
- [36] G. Deutscher and P. G. de Gennes, Proximity effects., Superconductivity. Parks, R. D. (ed.). New York, Marcel Dekker, Inc., 1969. 1, (1969).
- [37] M. C. de Ory, D. Rodriguez, M. T. Magaz, V. Rollano, D. Granados, and A. Gomez, Low loss hybrid nb/au superconducting resonators for quantum circuit applications (2024), 2401.14764 [quant-ph].
- [38] K. S. Il'in, A. Stockhausen, M. Siegel, A. D. Semenov, H. Richter, and H.-W. Hübers, Nbn heb for thz radiation: Technological issues and proximity effect, in *Proceedings* of the 19th International Symposium on Space Terahertz Technology, ISSTT 2008 (2008) pp. 367–372.
- [39] K. Il'in, M. Siegel, A. Semenov, A. Engel, and H. Hubers, Critical current of nb and nbn thin-film structures: The cross-section dependence, physica status solidi (c) 2, 1680–1687 (2005).
- [40] M. Tinkham, Introduction to Superconductivity, 2nd ed. (Dover Publications, Mineola, New York, 2004).
- [41] L. Sun, F. Dai, J. Zhang, J. Luo, C. Xie, J. Li, and H. Lei, The electrical resistivities of nanostructured aluminium

- films at low temperatures, Journal of Physics D: Applied Physics **50**, 415302 (2017).
- [42] R. Janninck and D. Whitmore, Electrical conductivity and thermoelectric power of niobium dioxide, Journal of Physics and Chemistry of Solids 27, 1183–1187 (1966).
- [43] S. Krause, V. Afanas'ev, V. Desmaris, D. Meledin, A. Pavolotsky, V. Belitsky, A. Lubenschenko, A. Batrakov, M. Rudziński, and E. Pippel, Ambient temperature growth of mono- and polycrystalline nbn nanofilms and their surface and composition analysis, IEEE Transactions on Applied Superconductivity 26, 1 (2016).
- [44] A. Zehnder, P. Lerch, S. P. Zhao, T. Nussbaumer, E. C. Kirk, and H. R. Ott, Proximity effects in nb/al-alox-al/nb superconducting tunneling junctions, Physical Review B 59, 8875 (1999).
- [45] N. Haberkorn, Y. Lee, C. Lee, J. Yun, F. Verón Lagger, M. Sirena, and J. Kim, Probing the quasiparticle relaxation time in ultrathin nbn microbridges via larkin-ovchinnikov instability near tc, ACS Applied Electronic Materials 10.1021/acsaelm.4c00629 (2024).
- [46] H. Du, Z. Xu, P. Zhang, D. Li, Z. Wei, Z. Wang, S. Hou, B. Chen, T. Liu, R. Liu, and et al., High-energy electron injection in top-gated niobium microbridges for enhanced power efficiency and localized control, Applied Physics Letters 124, 10.1063/5.0195254 (2024).
- [47] D. M. Glowacka, D. J. Goldie, S. Withington, H. Muhammad, G. Yassin, and B. K. Tan, Development of a NbN deposition process for superconducting quantum sensors, arXiv 10.48550/arXiv.1401.2292 (2014), 1401.2292 [physics.ins-det].
- [48] M. C. Salvadori, A. R. Vaz, R. J. Farias, and M. Cattani, Electrical resistivity of nanostructured platinum and gold thin films, Surface Review and Letters 11, 223–227 (2004).
- [49] J. R. Sambles, K. C. Elsom, and D. J. Jarvis, The electrical resistivity of gold films, Philosophical Transactions of the Royal Society of London. Series A, Mathematical and Physical Sciences 304, 365–396 (1982).
- [50] N. Joshi, A. Debnath, D. Aswal, K. Muthe, M. Senthil Kumar, S. Gupta, and J. Yakhmi, Morphology and resistivity of al thin films grown on si (111) by molecular beam epitaxy, Vacuum 79, 178–185 (2005).
- [51] L. A. Hall, Survey of electrical resistivity measurements on 16 pure metals in the temperature range 0 to 273 K, technical report (National Bureau of Standards, 1968).
- [52] A. He, S. Xu, A. Foroughi-Abari, and D. Karpuzov, Depth profiling of nbxo/w multilayers: Effect of primary ion beam species (o2+, ar+ and cs+), Surface and Interface Analysis 44, 934–937 (2012).
- [53] K. Komenou, T. Yamashita, and Y. Onodera, Energy gap measurement of niobium nitride, Physics Letters A 28, 335–336 (1968).
- [54] R. F. Averill, L. S. Straus, and W. D. Gregory, Tunneling measurements of the superconducting energy gap of bulk polycrystalline indium, Applied Physics Letters 20, 55–56 (1972).
- [55] R. A. Anderson and D. M. Ginsberg, Penetration depth and flux creep in thin superconducting indium films, Phys. Rev. B 5, 4421 (1972).
- [56] E. Maxwell and O. S. Lutes, Threshold field properties of some superconductors, Phys. Rev. 95, 333 (1954).